15th World Congress on Computational Mechanics (WCCM-XV)
8th Asian Pacific Congress on Computational Mechanics (APCOM-VIII)
Virtual Congress: 31 July – 5 August 2022
S. Koshizuka (Ed.)

MODELING FREELY FLYING MONARCH BUTTERFLIES USING A STRONGLY COUPLED HIGH FIDELITY NUMERICAL FRAMEWORK

JEREMY A. POHLY[1], CHANG-KWON KANG[2], TAEYOUNG LEE[3], AND HIKARU AONO[4]

[1]University of Alabama in Huntsville
Huntsville, AL, 35899, United States
jeremy.pohly@uah.edu

[2]University of Alabama in Huntsville
Huntsville, AL, 35899, United States
ck0025@uah.edu

[3] The George Washington University
Washington DC, 20052, United States
tylee@gwu.edu

[4] Shinshu University
Ueda, Nagano, 386-8567, Japan
aono@shinshu-u.ac.jp

Key words: Butterfly, Unsteady Aerodynamics, Flight Dynamics, Fluid Structure Interaction

Abstract. *Flying insects are impressive creatures due in part to their small size and agile flight maneuvers. Additionally, butterflies can be highly efficient fliers, as evidenced by monarchs having the longest migration amongst insects. To begin uncovering the complex mechanisms enabling monarchs to migrate roughly 80 million times their average body length, high-fidelity modeling tools are required: These tools must consider the distinguishing features of monarchs – their low flapping frequency, high Reynolds number (amongst insects), large wings relative to their body, low wing loading, flexibility of their wings, and the highly coupled interplay between the instantaneous wing aerodynamics and dynamic body response. Many butterfly flight models to date have neglected the passive wing pitching arising from butterfly's flexible wings. Here, we propose a framework that tightly couples the effects of all three physics solvers using a dynamic relaxation scheme. As such, the highly nonlinear interplay between fluid, body, and passive wing dynamics is efficiently accounted for in each time step. We apply the model to the free flight of monarch butterflies, resulting in stable motion for many periods without any controllers.*

1 INTRODUCTION

Flying insects have been the topic of study for many different disciplines in recent decades due to their small sizes and impressive aerial maneuverability [1]. Monarch butterflies stand

out amongst other insects due to their impressive migratory capabilities. In fact, the efficiency enabling their annual migration, which is the longest among insects, remains an unsolved mystery [2]. Like other insects, butterflies rely on flapping motions to generate lift which is enhanced due to several unsteady mechanisms [1,3–5]. They also have a large pair of flexible wings relative to their body [6] which flap at a low frequency $f \approx 10$ Hz compared to the flapping frequencies of hawkmoths ≈ 26 Hz [7], bumblebees ≈ 140 Hz [8], and fruit flies ≈ 230 Hz [9]. As a potential result of these features, the body motion of monarchs is closely coupled to the instantaneous aerodynamics and wing dynamics, which may not be the case for smaller insects with higher flapping frequency. This close coupling is manifested as translational undulations in the butterfly flight trajectory and large body pitch rotations occurring at frequencies very close to the flapping wing motion.

Many high-fidelity frameworks have been developed to model butterflies and uncover their unique flight characteristics [10–24]. However, none of these frameworks include all of the following capabilities, which can be essential for modeling freely flying butterflies: i) high-fidelity, unsteady aerodynamics at Reynolds numbers of $O(10^{3\text{-}4})$ to capture the insect-scale lift enhancing mechanisms; ii) multi-body dynamics of the wing-body system to capture the closely coupled interplay between body dynamics and wing aerodynamics iii) flexibility of the large wings to model the passively pitching wings; iv) strong coupling of all models to ensure numerical stability and efficiency of the fluid-structure-interaction (FSI); and v) anchoring of the coupled numerical model with experimental comparisons.

For example, none of the previous studies incorporate a strongly coupled wing flexibility model. Instead, one-way coupling of the aerodynamics, body dynamics, and passive pitch dynamics of the wing is often used, neglecting the two-way coupling effects. Additionally, many of the butterfly models [10,12,14–17] utilize an immersed boundary method to account for the no-slip condition on the moving wing surface. The accurate computation of the pressure on and vorticity near the wing surface is challenging using such methods at the Reynolds numbers relevant to butterflies. There have also been frameworks for tightly modeling the two-way coupling of fluid and body dynamics of insects in free flight, but do not include any passive wing pitch modeling [22,23].

The objective of this study is two-fold: i) first, we present a three-way tightly coupled numerical framework comprised of a high-fidelity 3D NS aerodynamics solver, a multi-body flight dynamics solver, and a torsional spring wing flexibility model; ii) we then apply experimentally measured monarch butterfly morphological parameters and kinematic inputs and compare the numerical results against the corresponding experimental results. We show that the high fidelity, tightly coupled model can generate flight trajectories that are qualitatively like those obtained for monarch butterflies in free flight.

2 METHODOLOGY

We consider a model butterfly (Fig. 1) that is comprised of a body, abdomen, and left and right wings, where the fore- and hind wings are combined into single wings of zero thickness. The left and right wings, along with the abdomen, are capable of motion relative to the butterfly body via spherical joints that attach them to the body. This framework was previously used in [25] for prescribed body pitch and wing pitch motion. Here, we allow for the body pitch to evolve as an additional unknown degree of freedom [21]. The body dynamics framework is

summarized in Section 2.2.

We are interested in modeling the passive pitch of the monarch wings too assess their effect on the resulting body dynamics. As such, a torsional spring is located at the wing root (Fig. 1b), such that the wing can passively pitch in the chordwise direction, about the torsional axis. This flexibility model is reflective of the setup used for experimentally characterizing the aeromechanics of passive wing rotation in flapping flight [26]. Previous numerical frameworks have been developed around such a physical setup [8,27,28], but they have not included the effects of the body dynamics, since they investigated the passive pitch effects in a hovering flight mode. The passive wing pitch model with body-dynamics terms is described in Section 2.3.

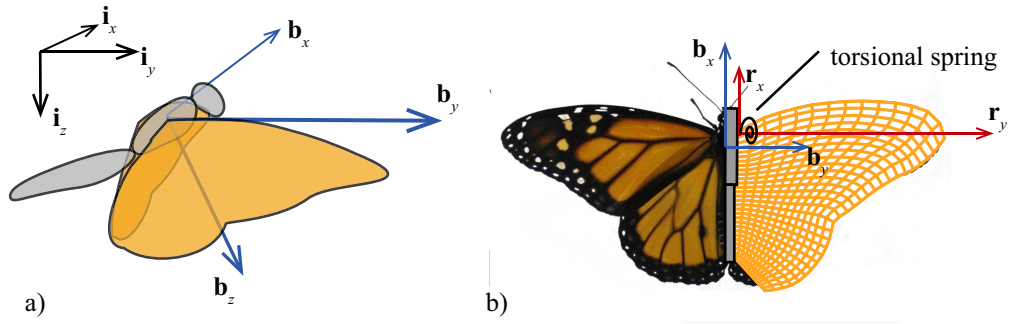

Figure 1: a) Schematic of a butterfly in free-flight with the inertial axis frame $\mathcal{F}_I$ in black and body-fixed frame $\mathcal{F}_B$ in blue. b) Representation of model with a cylindrical body and abdomen (gray), torsional spring along the $\mathbf{r}_y$ axis, and example surface mesh of the right wing used in CFD calculations.

For the aerodynamic modeling, the forces and moments are solved for the right wing only and consider left-right symmetry of forces and moments about the longitudinal plane to account for the left wing's aerodynamic contribution to the flight dynamics. The body and abdomen aerodynamic force calculations are neglected as they have been shown to be orders of magnitude less than the aerodynamic forces generated by the wings in forward flying butterflies [21]. Additionally, the body dynamics model includes the inertial effects of the left and right wings, body, and abdomen, as well as the aerodynamic force contributions of the left and right wings. The passive wing pitch dynamics include the aerodynamic and inertial forces of the wings, as well as the relative motion induced on the wings by the body motion. The strong coupling method is described in Section 2.4.

2.1 Aerodynamic Modeling

To accurately account for the unsteady, low-Reynolds number flow dynamics associated with the flapping wings, we directly solve the three-dimensional incompressible Navier-Stokes equations given by

$$\begin{aligned} \nabla \cdot V &= 0, \\ \rho \frac{\partial V}{\partial t} + \rho (V \cdot \nabla) V &= -\nabla p + \mu \nabla^2 V \end{aligned} \tag{1}$$

to determine the pressure $p \in \mathbb{R}$ and shear stress $\mu \nabla^2 V$ on the wing, where $\mu \in \mathbb{R}$ is the

dynamic viscosity coefficient of the fluid, and $V \in \mathbb{R}^3$ is the velocity field. These equations are solved using a well-validated structured, finite volume, pressure-based incompressible NS equation solver used extensively in flapping wing studies [29–32].

2.2 Multi-body Dynamics Modeling

To account for the coupling between the aerodynamics and body response, we use a multi-body dynamics solver that has previously been employed for monarch butterfly flight dynamic analysis [25]. A full description of the model derivation is shown in our previous work [25]. To define the multi-body dynamics, the three-dimensional special orthogonal group is denoted by $\mathrm{SO}(3) = \{R \in \mathbb{R}^{3\times3} \mid R^T R = I_{3\times3}, \det(R) = 1\}$, where $I_{3\times3} \in \mathbb{R}^{3\times3}$ is the identity matrix. The corresponding Lie algebra is $\mathrm{so}(3) = \{A \in \mathbb{R}^{3\times3} \mid A = -A^T\}$. The *hat* map $\wedge : \mathbb{R}^3 \to \mathrm{so}(3)$ is defined such that $\hat{x}y = x \times y$ for any $x, y \in \mathbb{R}^3$. Next $e_i \in \mathbb{R}^n$ denotes the i-th standard basis of $\mathbb{R}^n$ for an appropriate dimension n, e.g., $e_1 = (1,0,\ldots,0) \in \mathbb{R}^n$.

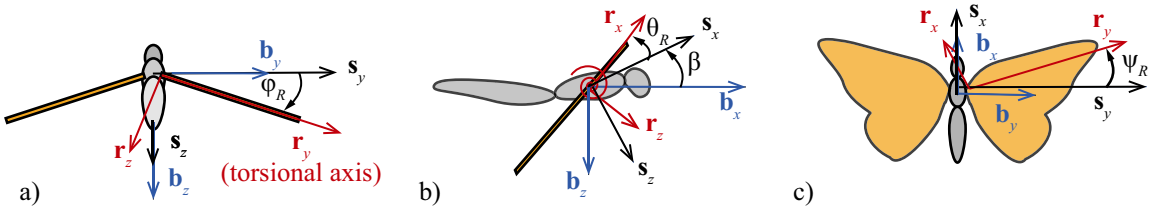

Figure 2: Right wing Euler angles: a) flapping φ_R, b) pitching θ_R and stroke plane β, c) deviation ψ_R.

Consider a flapping wing model that is composed of a body (combination of thorax and head), an abdomen, and two wings attached to the body (Fig. 1). Define an inertial frame $\mathcal{F}_I = \{\mathbf{i}_x, \mathbf{i}_y, \mathbf{i}_z\}$, which is compatible to the NED (north-east-down) frame (Fig. 1a). The various components of the model are summarized as follows.

- *Body*: The origin of the body-fixed frame $\mathcal{F}_B = \{\mathbf{b}_x, \mathbf{b}_y, \mathbf{b}_z\}$ is defined at the mass center of the body. Its attitude is given by $R \in \mathrm{SO}(3)$ and the position of the center of mass is given by $x \in \mathbb{R}^3$ in $\mathcal{F}_I$. The kinematics of the attitude is $\dot{R} = R\hat{\Omega}$, where $\Omega \in \mathbb{R}^3$ is the angular velocity of the body resolved in $\mathcal{F}_B$. The attitude of the body is defined as $R(t) = \exp(\theta_B \hat{e}_2)$, where θ_B is the pitch angle of the body.
- *Right wing*: Let $\mathcal{F}_R = \{\mathbf{r}_x, \mathbf{r}_y, \mathbf{r}_z\}$ be the frame fixed to the right wing at its root. Let $\mathcal{F}_S = \{\mathbf{s}_x, \mathbf{s}_y, \mathbf{s}_z\}$ be the stroke frame obtained by translating the origin of $\mathcal{F}_B$ to the center of the wing root and rotating it about $\mathbf{b}_y$ by $\beta \in [-\pi, \pi)$. Let $\mu_R \in \mathbb{R}^3$ be the fixed vector from the origin of $\mathcal{F}_B$ to that of $\mathcal{F}_R$. The attitude of the right wing relative to $\mathcal{F}_S$ namely $Q_R \in \mathrm{SO}(3)$ is described by 1-3-2 Euler angles $\varphi_R(t)$, $\theta_R(t)$, $\psi_R(t)$ (Fig. 2) as $Q_R = \exp(\beta\hat{e}_2)\exp(\varphi_R\hat{e}_1)\exp(-\psi_R\hat{e}_3)\exp(\theta_R\hat{e}_2)$, and its time derivative $\dot{Q}_R = Q_R\widehat{\Omega}_R$ for

$Q_R \in \mathbb{R}^3$.

- *Left wing*: Similarly, for the left wing, $Q_L = \exp(\beta\hat{e}_2)\exp(-\varphi_L\hat{e}_1)\exp(\psi_L\hat{e}_3)\exp(-\theta_L\hat{e}_2)$ with the set of Euler angles $\varphi_L(t)$, $\theta_L(t)$, $\psi_L(t)$, and $\dot{Q}_L = Q_L\widehat{\Omega}_L$ for $Q_L \in \mathbb{R}^3$.
- *Abdomen*: The abdomen is considered as a rigid body attached to the body via a spherical joint. The frame fixed to the abdomen is $\mathcal{F}_A = \{\mathbf{a}_x, \mathbf{a}_y, \mathbf{a}_z\}$, and its attitude relative to the body is denoted by $Q_A \in \mathrm{SO}(3)$ with $\dot{Q}_A = Q_A\widehat{\Omega}_A$ for $Q_A \in \mathbb{R}^3$. The attitude of the abdomen relative to the body is defined as $Q_A(t) = \exp(\theta_A\hat{e}_2)$.

The Euler-Lagrange equations of motion can be expressed as

$$\mathbf{J}_g(\dot{\xi}) - \mathrm{ad}^*_\xi \cdot \mathbf{J}_g(\xi) + \mathbf{L}_g(\xi)\xi = \mathbf{f}_a + \mathbf{f}_g + \mathbf{f}_\tau. \tag{2}$$

where $\xi = (\dot{x}, \Omega, \Omega_R, \Omega_L, \Omega_A)$, $\mathbf{J}_g(\xi)$ is the inertia tensor for the complete flapping wing vehicle, ad^*_ξ is the co-adjoint operator, $\mathbf{L}_g(\xi)$ represents the effects of the dependency of the inertia on the configuration, $\mathbf{f}_a$ and $\mathbf{f}_a$ are the aerodynamic and gravitational force and moment contributions, respectively, and $\mathbf{f}_\tau$ represents the control torque. The explicit expressions for the terms in the above equation are available in [25], where the present study considers the configuration for the prescribed flap and deviation angles of the wing as well as the abdomen angle: $\varphi_{R,L}(t)$, $\psi_{R,L}(t)$, θ_A. The pitch angles of the wing and body, $\theta_{R,L}$ and θ_B, as well as the position of the body center of mass x are the main solutions.

2.3 Passive Wing Pitch Dynamics Modeling

Torsional springs are located at the root of the right and left wings, such that the corresponding torsional axes are aligned with $\mathbf{r}_y$ and $\mathbf{l}_y$, respectively (as seen in Fig. 1b). The balance of the angular momentum in the rotating frame of the right wing $\mathcal{F}_R$ can be written as

$$\begin{bmatrix} F_{R,\mathrm{ext}} \\ T_{R,\mathrm{ext}} \end{bmatrix} = \begin{bmatrix} m_R I_{3\times3} & -m_R\hat{v}_R \\ m_R\hat{v}_R & J_R \end{bmatrix} \begin{bmatrix} \ddot{x}_R \\ \dot{\Omega}_{R,\mathrm{tot}} \end{bmatrix} + \begin{bmatrix} m_R\widehat{\Omega}_{R,\mathrm{tot}}\widehat{\Omega}_{R,\mathrm{tot}}v_R \\ \widehat{\Omega}_{R,\mathrm{tot}}J_R\Omega_{R,\mathrm{tot}} \end{bmatrix} \tag{3}$$

where $F_{R,\mathrm{ext}} = F_R \in \mathbb{R}^3$ is the aerodynamic force of the right wing in $\mathcal{F}_R$ and $T_{R,\mathrm{ext}} = M_R + \kappa_T\theta_R\hat{e}_2 \in \mathbb{R}^3$ is the summation of the right wing aerodynamic moments in $\mathcal{F}_R$ and κ_T is the torsional stiffness constant. Note that the LHS of Eq. (3) is related to the RHS of Eq. (2) as $\mathbf{f}_{a,7-9} = M_R$ and $\mathbf{f}_{a,1-3} = RQ_RF_R + RQ_LF_L + RQ_AF_A$ with F_L and $F_A \in \mathbb{R}^3$ being the aerodynamics forces of the left wing in $\mathcal{F}_L$ and abdomen in $\mathcal{F}_A$, respectively. The mass of the right wing is $m_R \in \mathbb{R}$, the inertia matrix of the right wing about the right wing origin in $\mathcal{F}_R$ is $J_R \in \mathbb{R}^{3\times3}$, the (translational) acceleration of the origin of the right wing in $\mathcal{F}_R$ is $\ddot{x}_R \in \mathbb{R}^3$, the wing center of mass location relative to the wing root in $\mathcal{F}_R$ is $v_R \in \mathbb{R}^3$, and the sum of the body rotation and the wing rotation in $\mathcal{F}_R$ is $\Omega_{R,\mathrm{tot}} \in \mathbb{R}^3$ with its time derivative being $\dot{\Omega}_{R,\mathrm{tot}} \in \mathbb{R}^3$.

The *y*-component of torque, resulting from evaluating this equation is

$$J_{R_{xy}}\left(\dot{\Omega}_{R,\mathrm{tot}_x}+\Omega_{R,\mathrm{tot}_y}\Omega_{R,\mathrm{tot}_z}\right)+J_{R_{yy}}\left(\dot{\Omega}_{R,\mathrm{tot}_y}-\Omega_{R,\mathrm{tot}_x}\Omega_{R,\mathrm{tot}_y}\right)-m_R\ddot{x}_{R_z}\nu_{R_x}=T_{\mathrm{ext}_y} \tag{4}$$

where $J_{R_{zz}}=J_{R_{xx}}+J_{R_{yy}}$, $J_{R_{xz}}=J_{R_{yz}}=0$ and $\nu_{R_z}=0$ due to the perpendiuclar axis theorem. The translational acceleration of the right wing in $\mathcal{F}_R$ is a result of the body translation and rotation and expressed as

$$\ddot{x}_R=Q_R^T[R^T\ddot{x}+(\dot{\Omega}+\widehat{\Omega}\Omega)\times\mu_R]\,. \tag{5}$$

Similarly, the right wing rotational acceleration is related to the body dynamics in $\mathcal{F}_R$ as

$$\dot{\Omega}_{R,\mathrm{tot}}=\dot{Q}_R^T\Omega+Q_R^T\dot{\Omega}+\dot{\Omega}_R\,. \tag{6}$$

Note that $\ddot{x}_R$ and Ω_R are dependent on the body accelerations $\ddot{x}$ and $\dot{\Omega}$ which result from solving the body dynamics equations of motion, Eqn. (2). The ODE for the wing structural dynamics can then be expressed in terms of the body-dynamics as

$$\ddot{\theta}_R=\frac{1}{J_{R_{yy}}}\left\{\begin{array}{l} M_{R_y}-\kappa_T\theta_R+\dots \\ J_{R_{yy}}\left[\begin{array}{l} -\ddot{\theta}_B c_{\varphi_R}c_{\psi_R}+\dot{\theta}_B\left(-2\dot{\varphi}_R s_{\theta R}c_{\psi_R}\left(c_{\varphi_R}c_{\theta_R}s_{\psi_R}-s_{\varphi_R}s_{\theta_R}\right)+\dot{\psi}_R\left(2c_{\varphi_R}c_{\theta_R}^2s_{\psi_R}-s_{\varphi_R}s_{2\theta_R}\right)\right)\dots \\ +\dot{\theta}_B^2\left(s_{\varphi_R}c_{\theta_R}+c_{\varphi_R}s_{\theta R}s_{\psi_R}\right)\left(c_{\varphi_R}c_{\theta_R}s_{\psi_R}-s_{\varphi_R}s_{\theta_R}\right)\dots \\ +\frac{1}{2}\left(\dot{\varphi}_R^2c_{\psi_R}^2-\dot{\psi}_R^2\right)s_{2\theta_R}-\ddot{\varphi}_R s_{\psi_R}-\dot{\varphi}_R\dot{\psi}_R c_{\psi_R}\left(1+c_{2\theta_R}\right) \end{array}\right]\dots \\ +J_{R_{xy}}\left[\begin{array}{l} \ddot{\theta}_B\left(c_{\varphi_R}c_{\theta_R}s_{\psi_R}-s_{\varphi_R}s_{\theta_R}\right)+\dot{\theta}_B\left(-2\dot{\varphi}_R c_{\varphi_R}s_{\theta_R}c_{\psi_R}^2+\dot{\psi}_R\left(2c_{\varphi_R}c_{\theta_R}c_{\psi_R}\right)\right)\dots \\ +\dot{\theta}_B^2\left(s_{\varphi_R}c_{\theta_R}+c_{\theta_R}s_{\theta_R}s_{\psi_R}\right)c_{\varphi_R}c_{\psi_R}\dots \\ -\ddot{\varphi}_R c_{\varphi_R}c_{\psi_R}-\ddot{\psi}_R s_{\theta_R}-\frac{1}{2}\dot{\varphi}_R^2 s_{\theta_R}s_{2\psi_R}+2\dot{\varphi}_R\dot{\psi}_R c_{\theta_R}s_{\psi_R} \end{array}\right]\dots \\ +m_R\nu_{R_x}\left[\begin{array}{l} s_{\beta+\theta_B}\left(\ddot{x}_x c_{\varphi_R}c_{\theta_R}-s_{\theta_R}\left(\ddot{x}_z c_{\psi_R}+\ddot{x}_x s_{\varphi_R}s_{\psi_R}\right)\right)+c_{\beta+\theta_B}\left(\ddot{x}_z c_{\varphi_R}c_{\theta_R}+s_{\theta_R}\left(\ddot{x}_x c_{\psi_R}-\ddot{x}_z s_{\varphi_R}s_{\psi_R}\right)\right)\dots \\ +\mu_{R_x}\ddot{\theta}_B\left(s_\beta s_{\theta_R}c_{\psi_R}-c_\beta c_{\varphi_R}c_{\theta_R}+c_\beta s_{\varphi_R}s_{\theta_R}s_{\psi_R}\right) \end{array}\right] \end{array}\right\} \tag{7}$$

Note that when the body-related terms are set to zero, the expression dervied in [8] is recovered (aside from the sign differences wing axis choices).

2.4 Coupling Strategy

We implement a two-way, strongly coupled scheme for imposing the effects of the aerodynamics (Eqn. (1), body motion (Eqn. (2)), and wing motion (Eqn. (7)) on each other to accurately model the fluid structure interaction (FSI). The approach is based on a time-domain partitioned solution process in which the nonlinear differential equations governing the fluid, structure, and flight dynamics are solved independently and spatially coupled through the interface between the fluid and the structure as well as the passive pitch angle of the wing. At

each time step, the fluid, structural and flight dynamic equations of motion solvers are called one after the other until sufficient convergence on the displacements of the shared interface is met via inner FSI iterations before advancing to the next time step.

The schematic in Fig. 3 describes the details of the FSI scheme, where the states are the right wing pitch Euler angle $\Theta = [\theta_R]$ for the wing structural dynamics and the longitudinal body position and pitch angle $\chi = [x, z, \theta_B]^T$ for the body dynamics. The time step iterations are denoted by n and the inner FSI iterations are denoted by k. To accelerate convergence, the Aitken relaxation method [33] is implemented. The FSI-coupling for partitioned domains can be summarized for the FSI-interface Γ as $\tilde{w}_{\Gamma,n+1} = S_\Gamma^{-1}\left[F_\Gamma\left(w_{\Gamma,n+1}\right)\right]$, where F_Γ denotes the fluid solver, S_Γ denotes the structural solver, and $w_{\Gamma,n+1}$ is the displacement of the interface Γ at the next time level n+1, and $\tilde{w}_{\Gamma,n+1}$ is the displacement output from the structural solver. Time integration is achieved using a semi-implicit Newmark-Beta integration scheme.

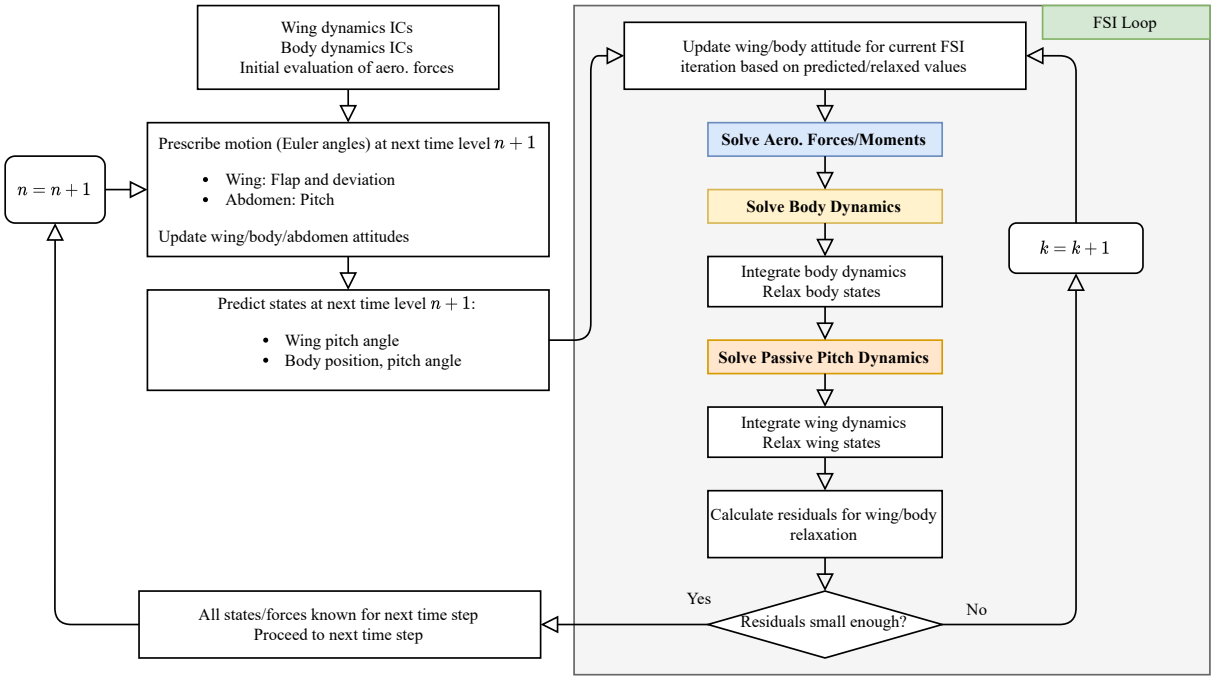

Figure 3: Tightly coupled FSI scheme for convergence between the flow field, body, and wing pitch dynamics.

2.5 Validation of Coupled Aerodynamic and Passive Wing Pitch Without Body Motion

The coupling between the unsteady wing aerodynamics and torsional spring dynamics is validated by comparing the passive pitch wing angle and the lift against two data from the literature: experimental measurements by Whitney and Wood [26] and numerical solutions by Kolomenskiy et al. [8]. Here, we compare the present numerical framework to the 'short hinge' case of Whitney and Wood [26], where no body motion is imposed. In this case the body-related velocities and accelerations in Eqn. (7) become zero. There is a close agreement between the three solutions as seen in Fig. 4.

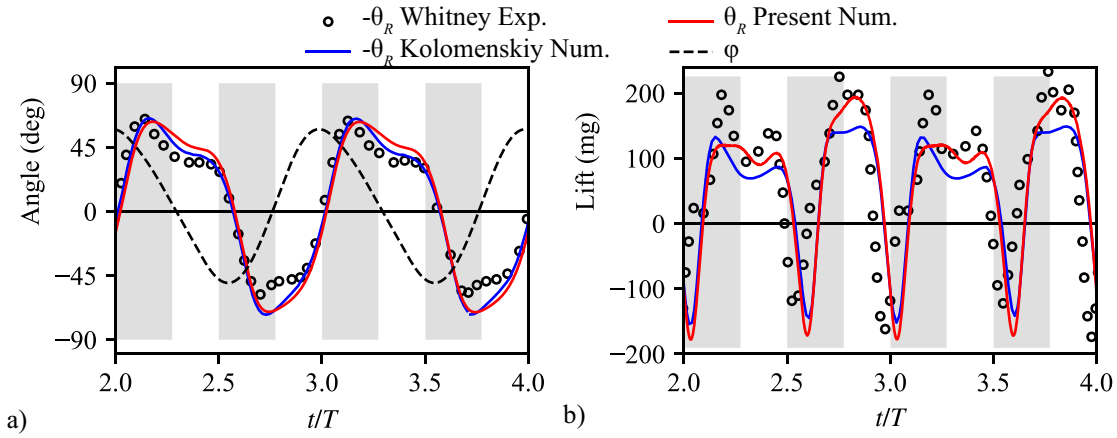

Figure 4: a) Passive pitch θ angle and b) lift for the present framework compared to [8,26].

2.6 Experimental Data Reduction of Climbing Monarchs

Freely flying monarch butterflies were tracked using a VICON motion tracking system [25,34]. A sample butterfly with tracking markers and 3D reconstruction ca be found in Fig. 5a,b. The resulting climbing trajectories of a single monarch can be found in Fig. 5c, which are used as reference cases for the numerical model results. The corresponding wing kinematics for the flapping and pitching of the nine trajectories, along with their ensemble average values (black) and Fourier representations (red dashed) can be found in Fig. 6. Similar time histories were also generated for the body and abdomen pitch values, θ_B and θ_A, respectively.

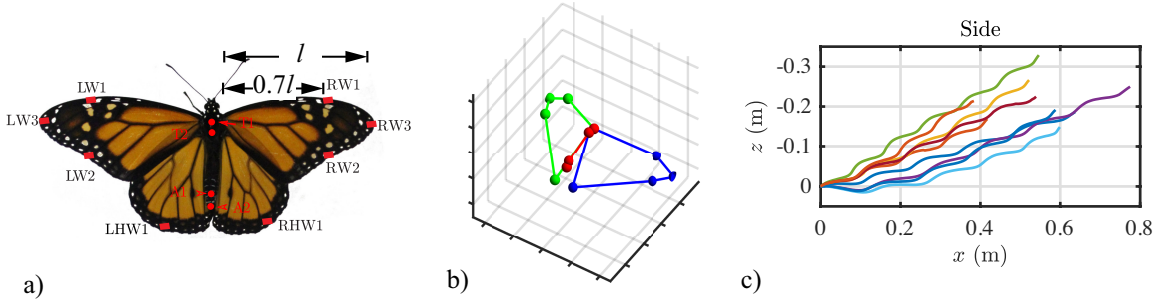

Figure 5: a) Generic monarch with markers, b) 3D marker reconstruction, and c) climbing trajectories.

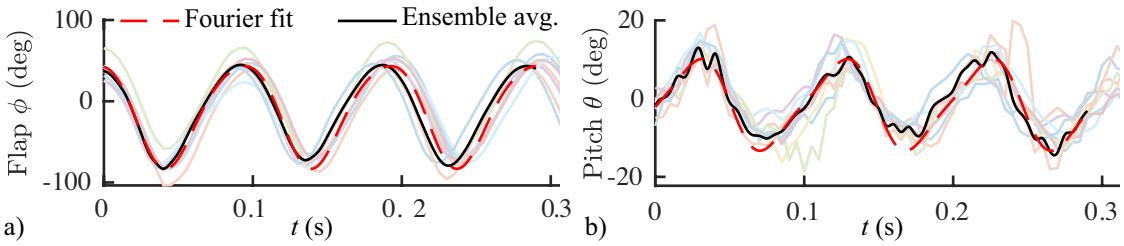

Figure 6: a) Flapping and b) pitching angles from nine experimental recordings.

2.7 Model Inputs

The Fourier coefficients for wing flapping and deviation, along with the abdomen pitch angle were taken from the experimental data and applied to the monarch simulation. The additional kinematic and morphological inputs used for the simulations are found in Table 1.

Table 1: Morphological and kinematics variables used for monarch simulations.

Param.	Description	Value	Units	Param.	Description	Value	Units
f	flapping frequency	10.2	Hz	m_B	body mass	0.22	mg
β	stroke plane angle	25.4	deg	m_A	abdomen mass	25.39	deg
l	single wingspan	5.2	cm	m_R	right wing mass	3.535 – 3.725	mg
S	single wing area	15.2	cm^2	κ_T	torsional spring const.	0.15	mN-m

The simulations were run with an FSI tolerance of 1×10^{-8} and an initial velocity of $\dot{x} = \left[1.3, 0.0, -0.562\right]^T$ m/s. All wing and body states were prescribed for the first 10 time steps before beginning the time integration of the body and wing equations of motion.

3 RESULTS AND DISCUSSION

A design space was run around the nominal monarch values obtained and described in Section 2.6. The primary design variable is the wing mass m_R. A change in the wing mass affects the total mass as well as the wing moments of inertia, which, in turn, have effects on both the body and wing dynamics. The wing mass m_R was varied between 3.535 and 3.725 mg.

3.1 Trajectories

Below are the resulting trajectories from the design space which varied the wing mass. Results for all cases can be found in Fig. 7a, where the case that most closely matches the experimental trajectories (m_R=3.625 mg) is highlighted in red and plotted against the experimental measurements in Fig. 7b. It can be seen in Fig. 7b that the body undulation amplitude, frequency, and climb angle closely match those of the experiments.

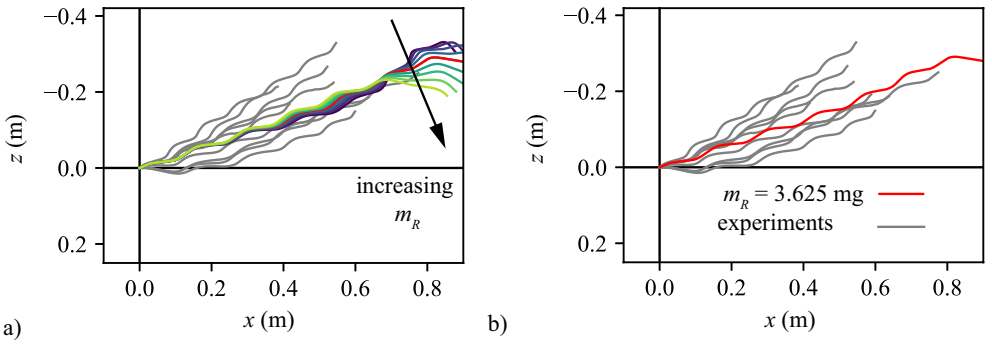

Figure 7: a) All trajectories and b) "best" trajectory for simulated monarch compared to experiments.

3.2 Forces and Passive Pitching Angles

There is very good agreement between the simulation and experiments with respect to the forces in the body frame (Fig. 8a,b), as well as the passive pitch angles of the wing and body (Fig. 8c,d). This indicates that model captures the necessary features for simulating dimensional monarch butterfly flight trajectories. Note that the simulation is only shown for six flapping cycles, after which a pitch instability results in a sever pitch down motion due to the open-loop nature of this simulation.

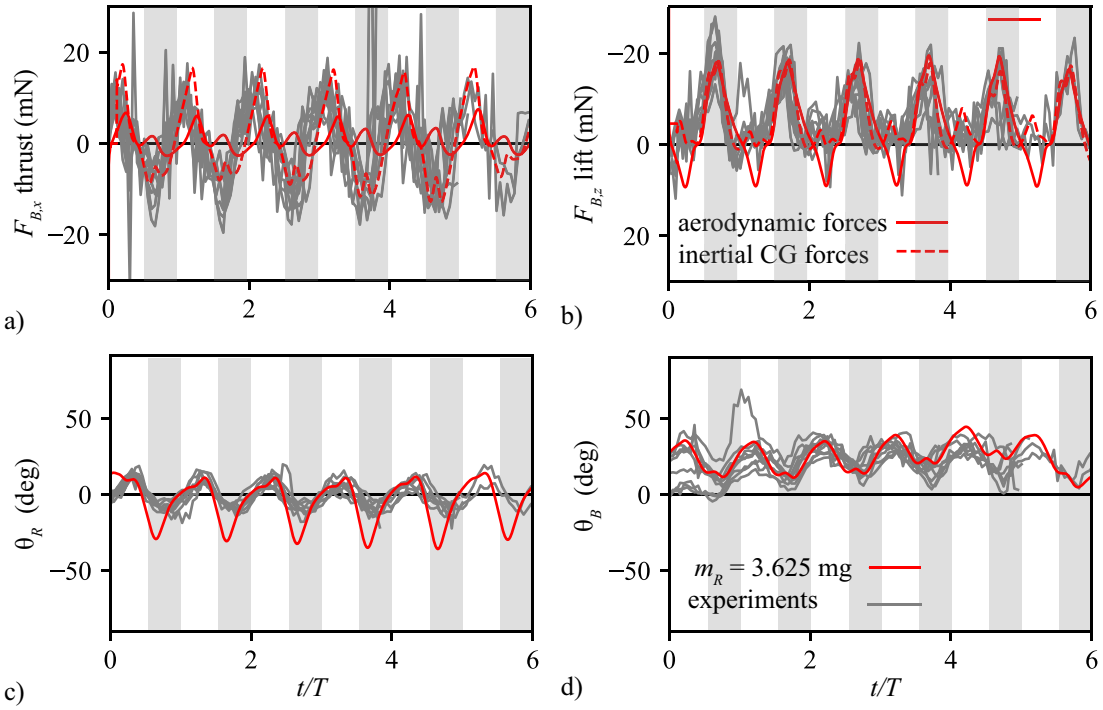

Figure 8: a) Thrust, b) lift, c) passive right wing, and d) passive body pitching angles.

3.3 Visualization of Flow Structures, Surface Pressure, and Flight Path

Example flow field visualization is shown in Fig. 9 at the upstroke position at $t/T = 0.5$ in Fig. 9a and the downstroke position, starting a new flapping period at $t/T = 3.0$ in Fig. 9b. The trajectory of the simulation is shown in red which tracks the time history of the body CG. This is compared to the black traces which are the experimental measurements of the CG location of the monarch butterfly across nine trials (Section 2.6). There is close agreement in both the flight path angle and amplitude of the body undulations between the simulation and experiment, as also demonstrated in Fig. 7. The vortex dynamics are visualized by the iso-Q surfaces which are colored by the vorticity magnitude along $\mathbf{r}_y$. Additionally, the wing surfaces are colored by the coefficient of pressure, revealing that the coherent large-scale vortices generate low pressure regions and pressure gradients on the wing surface.

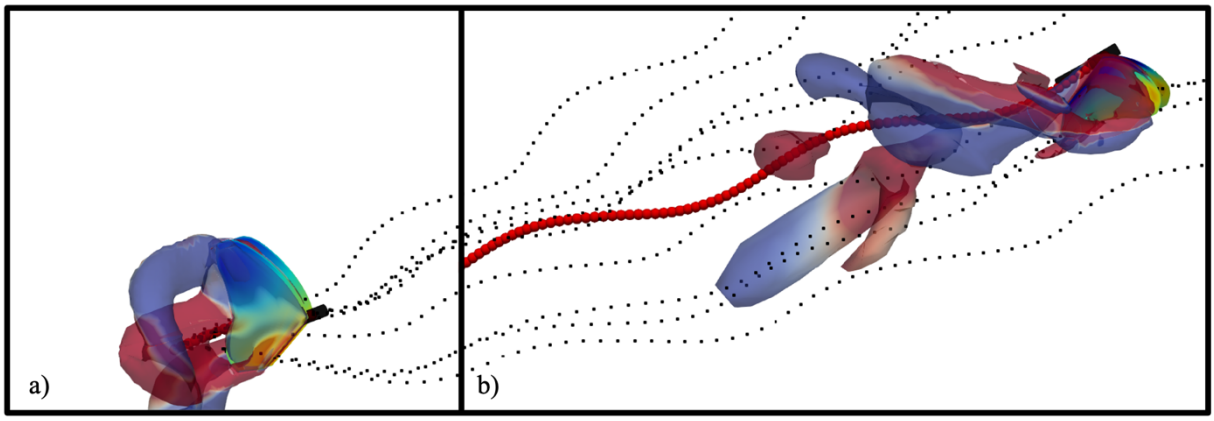

Figure 9: Visualization of vortical structures and surface pressure coefficient at a) $t/T = 0.5$ and b) 3.0.

4 CONCLUSIONS

- A three-way strongly coupled framework has been established for modeling the passive wing and body pitch of freely flying monarch butterflies.
- The model tightly couples unsteady NS aerodynamic solutions to a multi-body dynamics solver and a Newton-Euler-based passive wing pitch dynamics solver.
- Good agreement is found between numerical simulations and experimental measurements for a climbing monarch butterfly with passive wing pitch.

REFERENCES

[1] Shyy, W., Aono, H., Kang, C.-K., and Liu, H., *An Introduction to Flapping Wing Aerodynamics*, New York, NY: Cambridge University Press, 2013.
[2] Brower, L., "Monarch Butterfly Orientation: Missing Pieces of a Magnificent Puzzle," *Journal of Experimental Biology*, Vol. 199, Nr. 1, 1996, pp. 93–103.
[3] Dickinson, M. H., Lehmann, F.-O., and Sane, S. P., "Wing Rotation and the Aerodynamic Basis of Insect Flight," *Science*, Vol. 284, Nr. 5422, 1999, pp. 1954–1960.
[4] Ellington, C. P., van den Berg, C., Willmott, A. P., and Thomas, A. L. R., "Leading-Edge Vortices in Insect Flight," *Nature*, Vol. 384, Nr. 6610, 1996, pp. 626–630.
[5] Srygley, R. B., and Thomas, A. L. R., "Unconventional Lift-Generating Mechanisms in Free-Flying Butterflies," *Nature*, Vol. 420, Nr. 6916, 2002, pp. 660–664.
[6] Kodali, D., Medina, C., Kang, C. K., and Aono, H., "Effects of Spanwise Flexibility on the Performance of Flapping Flyers in Forward Flight," *Journal of the Royal Society Interface*, Vol. 14, Nr. 136, 2017.
[7] Liu, H., Ellington, C. P., Kawachi, K., Van Den Berg, C., and Willmott, A. P., "A Computational Fluid Dynamic Study of Hawkmoth Hovering," *Journal of Experimental Biology*, Vol. 201, Nr. 4, 1998, pp. 461–477.
[8] Kolomenskiy, D., Ravi, S., Xu, R., Ueyama, K., Jakobi, T., Engels, T., Nakata, T., Sesterhenn, J., Schneider, K., Onishi, R., and Liu, H., "The Dynamics of Passive Feathering Rotation in Hovering Flight of Bumblebees," *Journal of Fluids and Structures*, Vol. 91, 2019.
[9] Fry, S. N., Sayaman, R., and Dickinson, M. H., "The Aerodynamics of Free-Flight Maneuvers in Drosophila," *Science*, Vol. 300, Nr. 5618, 2003, pp. 495–498.
[10] Senda, K., Obara, T., Kitamura, M., Yokoyama, N., Hirai, N., and Iima, M., "Effects of Structural Flexibility of Wings in Flapping Flight of Butterfly," *Bioinspiration & biomimetics*, Vol. 7, Nr. 2, 2012, p. 25002.
[11] Huang, H., and Sun, M., "Forward Flight of a Model Butterfly: Simulation by Equations of Motion Coupled with the Navier-Stokes Equations," *Acta Mechanica Sinica*, Vol. 28, Nr. 6, 2012, pp. 1590–1601.
[12] Suzuki, K., Minami, K., and Inamuro, T., "Lift and Thrust Generation by a Butterfly-like Flapping Wing–Body Model: Immersed Boundary–Lattice Boltzmann Simulations," *Journal of Fluid Mechanics*, Vol. 767, 2015, pp. 659–695.
[13] Fei, Y. H. J., and Yang, J. T., "Importance of Body Rotation during the Flight of a Butterfly," *Physical Review*

E, Vol. 93, Nr. 3, 2016, pp. 1–10.
[14] Jayakumar, J., Senda, K., and Yokoyama, N., "Control of Pitch Attitude by Abdomen During Forward Flight of Two-Dimensional Butterfly," *Journal of Aircraft*, Vol. 55, Nr. 6, 2018, pp. 2327–2337.
[15] Suzuki, K., Okada, I., and Yoshino, M., "Effect of Wing Mass on the Free Flight of a Butterfly-like Model Using Immersed Boundary-Lattice Boltzmann Simulations," *Journal of Fluid Mechanics*, Vol. 877, 2019, pp. 614–647.
[16] Suzuki, K., Aoki, T., and Yoshino, M., "Effect of Chordwise Wing Flexibility on Flapping Flight of a Butterfly Model Using Immersed-Boundary Lattice Boltzmann Simulations," *Physical Review E*, Vol. 100, Nr. 1, 2019, pp. 1–16.
[17] Suzuki, K., and Yoshino, M., "A Trapezoidal Wing Equivalent to a Janatella Leucodesma's Wing in Terms of Aerodynamic Performance in the Flapping Flight of a Butterfly Model," *Bioinspiration and Biomimetics*, Vol. 14, Nr. 3, 2019.
[18] Bode-Oke, A. T., and Dong, H., "The Reverse Flight of a Monarch Butterfly (Danaus Plexippus) Is Characterized by a Weight-Supporting Upstroke and Postural Changes," *Journal of the Royal Society Interface*, Vol. 17, Nr. 167, 2020.
[19] Lin, Y., Chang, S., Lai, Y., and Yang, J.-T., "Beneficial Wake-Capture Effect for Forward Propulsion with a Restrained Wing-Pitch Motion of a Butterfly," *Royal Society Open Science*, Vol. 8, Nr. 8, 2021, p. 202172.
[20] Zhang, Y., Wang, X., Wang, S., Huang, W., and Weng, Q., "Kinematic and Aerodynamic Investigation of the Butterfly in Forward Free Flight for the Butterfly-Inspired Flapping Wing Air Vehicle," *Applied Sciences (Switzerland)*, Vol. 11, Nr. 6, 2021.
[21] Chang, S., Lai, Y., Lin, Y., and Yang, J., "Enhanced Lift and Thrust via the Translational Motion between the Thorax-Abdomen Node and the Center of Mass of a Butterfly with a Constructive Abdominal Oscillation," *Physical Review E*, Vol. 102, Nr. 6, 2020, p. 062407.
[22] Zheng, L., Hedrick, T. L., and Mittal, R., "Time-Varying Wing-Twist Improves Aerodynamic Efficiency of Forward Flight in Butterflies," *PLoS ONE*, Vol. 8, Nr. 1, 2013, pp. 1–10.
[23] Yokoyama, N., Senda, K., Iima, M., and Hirai, N., "Aerodynamic Forces and Vortical Structures in Flapping Butterfly's Forward Flight," *Physics of Fluids*, Vol. 25, Nr. 2, 2013, p. 021902.
[24] Fei, Y. H. J., and Yang, J. T., "Enhanced Thrust and Speed Revealed in the Forward Flight of a Butterfly with Transient Body Translation," *Physical Review E - Statistical, Nonlinear, and Soft Matter Physics*, Vol. 92, Nr. 3, 2015, pp. 1–10.
[25] Tejaswi, K. C., Sridhar, M. K., Kang, C., and Lee, T., "Effects of Abdomen Undulation in Energy Consumption and Stability for Monarch Butterfly," *Bioinspiration & Biomimetics*, Vol. 16, Nr. 4, 2021, p. 046003.
[26] Whitney, J. P., and Wood, R. J., "Aeromechanics of Passive Rotation in Flapping Flight," *Journal of Fluid Mechanics*, Vol. 660, 2010, pp. 197–220.
[27] Lei, M., and Li, C., "The Aerodynamic Performance of Passive Wing Pitch in Hovering Flight," *Physics of Fluids*, Vol. 32, Nr. 5, 2020.
[28] Zeyghami, S., Zhong, Q., Liu, G., and Dong, H., "Passive Pitching of a Flapping Wing in Turning Flight," *AIAA Journal*, Vol. 57, Nr. 9, 2019, pp. 3744–3752.
[29] Tang, J., Viieru, D., and Shyy, W., "Effects of Reynolds Number and Flapping Kinematics on Hovering Aerodynamics," *AIAA Journal*, Vol. 46, Nr. 4, 2008, pp. 967–976.
[30] Shyy, W., Aono, H., Chimakurthi, S. K., Trizila, P., Kang, C.-K., Cesnik, C. E. S., and Liu, H., "Recent Progress in Flapping Wing Aerodynamics and Aeroelasticity," *Progress in Aerospace Sciences*, Vol. 46, Nr. 7, 2010, pp. 284–327.
[31] Pohly, J., Salmon, J., Bluman, J., Nedunchezian, K., and Kang, C.-K., "Quasi-Steady versus Navier–Stokes Solutions of Flapping Wing Aerodynamics," *Fluids*, Vol. 3, Nr. 4, 2018, p. 81.
[32] Pohly, J. A., Kang, C., Landrum, D. B., Bluman, J. E., and Aono, H., "Data-Driven CFD Scaling of Bioinspired Mars Flight Vehicles for Hover," *Acta Astronautica*, Vol. 180, Nr. October 2020, 2021, pp. 545–559.
[33] Küttler, U., and Wall, W. A., "Fixed-Point Fluid-Structure Interaction Solvers with Dynamic Relaxation," *Computational Mechanics*, Vol. 43, Nr. 1, 2008, pp. 61–72.
[34] Kang, C., Cranford, J., Sridhar, M. K., Kodali, D., Landrum, D. B., and Slegers, N., "Experimental Characterization of a Butterfly in Climbing Flight," *AIAA Journal*, Vol. 56, Nr. 1, 2018, pp. 15–24.